Contribution of calving to frontal ablation quantified from seismic and hydroacoustic observations calibrated with lidar volume measurements

Andreas Köhler[1], Michał Pętlicki [2], Pierre-Marie Lefeuvre [1], Giuseppa Buscaino [3], Christopher Nuth [1], and Christian Weidle[4]

[1]Department of Geosciences, University of Oslo, Post Box 1047, 0316 Oslo, Norway
[2]Centro de Estudios Científicos, Valdivia, Chile
[3]Institute for Coastal Marine Environment IAMC CNR
[4]Institute of Geosciences, Christian-Albrechts-Universität zu Kiel, Kiel, Germany

Correspondence: Andreas Köhler (andreas.kohler@geo.uio.no, andreas.koehler.geo@gmail.com)

Abstract. Frontal ablation contributes significantly to the mass balance of tidewater glaciers in Svalbard and can be recovered with high temporal resolution using continuous seismic records. Determination of the relative contribution of dynamic ice loss through calving to frontal ablation requires precise estimates of calving volumes at the same temporal resolution. We combine seismic and hydroacoustic observations close to the calving front of Kronebreen, a marine terminating glacier in Svalbard, with

5 repeat lidar scanning of the glacier front. Simultaneous time-lapse photography is used to assign volumes measured from lidar scans to seismically detected calving events. Empirical models derived from signal properties such as integrated amplitude are able to replicate volumes of individual calving events and cumulative subaerial ice loss over different lidar scan intervals from seismic and hydroacoustic data alone. This enables quantification of the contribution of calving to frontal ablation, which we estimate for Kronebreen to be about 18-30%, slightly below the subaerially exposed area of the glacier front. We further

10 develop a model calibrated for the permanent seismic station KBS at about 15 km distance from the glacier front, where 15-60% of calving events can be detected under variable noise conditions due to reduced signal amplitudes at distance. Between 2007 and 2017, we find a 5-30% contribution of calving ice blocks to frontal ablation which emphasizes the importance of underwater melting (roughly 150–350 m a^{-1}). This study shows the feasibility to seismically monitor not only frontal ablation rates but also its dynamic ice loss contribution continuously and at high temporal resolution.

1 Introduction

Glaciers are an important contributor to eustatic sea level rise in a warming climate (Gardner et al., 2013; Huss and Hock, 2015), with dynamic discharge one of the largest uncertainties in future predictions (Vaughan et al., 2013). Frontal ablation at marine-terminating glaciers comprises ice loss through subaerial and submarine melting and iceberg calving. Submarine melting strongly promotes calving through thermal undercutting (Bartholomaus et al., 2013; Luckman et al., 2015; Vallot

20 et al., 2018; How et al., 2019). To monitor and better understand the dynamic ice loss contribution, field records of calving can be obtained visually through human observation and time-lapse imagery (e.g., O'Neel et al., 2003; Chapuis et al., 2010; How

et al., 2019), as well as through terrestrial remote sensing such as ground-based radar and lidar surveys. Calving events are also successfully detected from passive indirect techniques such as seismic (Ekström et al., 2003; Amundson et al., 2008; O'Neel et al., 2010; Walter et al., 2012; Bartholomaus et al., 2012; Köhler et al., 2015) and hydroacoustic monitoring (Glowacki et al.,

5   2015).

Seismic and hydroacoustic methods have the advantage to produce continuous calving records with high temporal resolution and limited logistical effort. Furthermore, they are independent of visibility conditions in contrast to optical methods. However, inferring ice volumes from those signals using physical models is challenging (Podolskiy and Walter, 2016; Aster and Winberry, 2017). For example, it requires different approaches dependent on the calving style, i.e., for glacial earthquake signals

10   from tabular iceberg calving such as observed in Greenland (e.g., Murray et al., 2015) or for seismic calving signals generated during iceberg impact on the sea surface (Bartholomaus et al., 2012). The only successful approach so far is calibrating seismic records to directly inferred calving sizes using empirical models valid for a particular glacier and recording site for the latter type of calving. For example, Bartholomaus et al. (2015) developed an empirical model to estimate iceberg volumes from individual seismic calving signals at Yahtse glacier, Alaska based upon visually perceived iceberg sizes (quantified on an

15   integer scale). Köhler et al. (2016) calibrated an empirical model of dynamic ice loss using frontal glacier ablation measured through timeseries of repeat satellite images, allowing reconstruction of frontal ablation directly from seismic calving signals with weekly resolution and going back decades. In this approach, a constant ratio between frontal melting and calving was implicitly included, an assumption that requires validation through independent dynamic ice loss measurements.

In this study, we measure dynamic ice loss at Kronebreen (Svalbard) using seismic data recorded at three locations and

20   precise ice volume measured from repeat lidar scanning for calibration, instead of visually perceived calving size empirically scaled to ice volume (Bartholomaus et al., 2012). In addition, we use for the first time a hydroacoustic record for calibration in addition to seismic data. Our method relies on time-lapse camera images to prepare the calibration data set. Finally, we compare our results with independently measured frontal ablation rates at Kronebreen to assess the potential to quantify the contribution of frontal melting.

25   ## 2   Study site and calving records

Kronebreen is a grounded tidewater glacier in the northwestern part of the Arctic archipelago of Svalbard ($78.88\,°$N, $12.55\,°$E) about $15\,$km East of the research settlement of Ny Ålesund. Mass loss is dominated by frontal ablation (Nuth et al., 2012; Luckman et al., 2015) making it an ideal candidate to further understand the processes of calving and frontal ablation. The glacier is currently experiencing an accelerated, rapid retreat with more than $1\,$km since 2012 (Schellenberger et al., 2015;

30   Köhler et al., 2016; Deschamps-Berger et al., 2019) with considerable future implications for the fjord ecosystem (Torsvik et al., 2019). At the end of August 2016 a multi-disciplinary field campaign was carried out to measure the calving front of Kronebreen continuously over a two-week period with simultaneous acquisitions from time-lapse cameras, a lidar scanner, terrestrial radar interferometry, passive seismic, and hydroacoustic arrays (Nuth et al, in preparation).

2.1 Seismic data

Between 24 August and 2 September 2016, a temporary seismic network was deployed in the vicinity of the marine terminus of Kronebreen (Fig. 1c, Köhler et al., 2019). Eleven 4.5 Hz three-component geophones connected to Omnirecs DATA-CUBE data loggers operating with a sampling frequency of 100 Hz were arranged as two small-aperture arrays to the North (KRBN, four stations) and South (KRBS, seven stations) of the calving front of Kronebreen. The inter-station spacings of both arrays were between 120 and 780 m. During installation shallow holes were dug in the ground to accommodate the geophones. Instruments were covered with soil and the data loggers were placed at the surface. Each DATA-CUBE used two internal 1.5 V batteries as power supply which were exchanged once during the survey. We also used the continuous, long-time record of the permanent broadband Kings Bay station (KBS) in Ny-Ålesund at 15 km distance from Kronebreen which operated with a sampling frequency of 40 Hz.

2.2 Hydroacoustic data

The field experiment included measurements of the underwater acoustic soundscape close to the terminus of Kronebreen. Three underwater acoustic recorders were deployed at about 45 m water depth with the hydrophones placed 10 m above the sea bottom. The acoustic data were collected from 26 August to 3 September 2016. We used autonomous recorders (SM2, Wildlife Acoustics, US) with a hydrophone recording bandwidth of 8 Hz to 150 kHz and sensitivies of -166 $\pm$ 1 dB re 1 V/μ Pa in the band from 100 Hz to 15 kHz. A 35 kg weight resting on the sea bottom and a small sub-surface buoy above the instrument were used to maintain the vertical alignment. The buoy was connected to the upper part of the recorder with a thin, 2 m long rope. All the components were connected with non-metallic ropes to avoid noise due to moving parts. We sampled continuously (duty cycle of 100%) with a sampling frequency of 192 kHz and a resolution of 16 bits. No pre-amplification or filtering was applied during the recordings except for the automatic anti-aliasing filter. The recording unit was recovered using an acoustic releaser. The locations of hydrophones ACB and ACC are shown in Fig. 1c.

2.3 Time-lapse camera image data

A time-lapse camera was installed on a tripod at the top of a moraine cone at 8 m a.s.l. (see Fig. 1c). The Harbotronics set consisted of a sealed box, an intervalometer, a camera (see Table A1) and an external 12 V 30 A battery. The camera was set to take a picture every 2 seconds, but the frequency varied due to a combination of factors related to the camera, SD card, shutter speed, battery, and temperature. The lens and focus were taped to the lowest focal length (i.e. 18 mm) in order to cover the largest part of the glacier front. The aperture was fixed to a value of 8.0 whereas the ISO and shutter speed were automatically adjusted to adapt to the ambient luminosity. The time-lapse camera was visited every one or two days to replace the SD card and correct for any clock-drift.

The time-lapse images are preprocessed and then used to identify calving events. For visual inspection, we extract the corresponding images within one minute around each calving event detected in the seismic record to generate an animated image sequence. Only a few percent of all events visible in the time-lapse images represent submarine calving, similar to
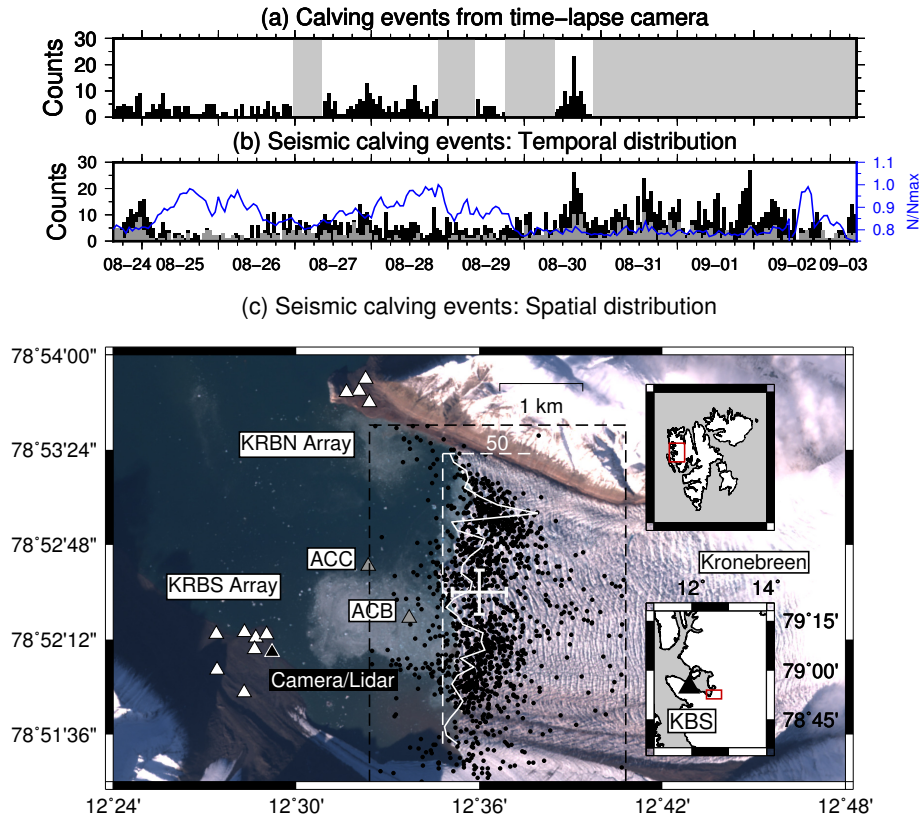
Figure 1. Calving event time series and location. (a) Hourly counts of calving events automatically detected on time-lapse camera images. Grey areas indicate image gaps. (b) Hourly counts of seismic detections simultaneously at KRBN and KRBS (black) and at KBS (gray). Blue line shows relative variations in seismic background noise level (N) with respect to maximum level (Nmax) in recording period. (c) Triangles show locations of time-lapse camera (black), Lidar scanner (black), seismic (white), and hydroacoustic (gray) instruments at the calving front of Kronebreen. Black points are seismic calving event locations. White error bars show an estimate of the typical location uncertainty. White curve is histogram of time-lapse camera event counts projected on a line (dashed) parallel to the terminus. Dashed box is used to classify located seismic signals as calving events. Insets to the right show Arctic archipelago of Svalbard (upper) and a closeup map of Kongsfjorden area (lower) with location of permanent broadband seismometer KBS in Ny-Ålesund.

observations at other glaciers in Svalbard (How et al., 2019). In addition, an autonomous calving event detector is implemented to compare the time series of seismicity and directly observed calving (see Fig. 1a). A detailed description of the image processing and the calving detection algorithm can be found in the Appendix (Fig. A1, Table A1).

2.4 Repeat lidar scanning

Volumes of individual and aggregated calving events were calculated by differencing Digital Surface Models (DSMs) obtained from repeat lidar scanning of the glacier terminus. The glacier front and surroundings were surveyed with a long-range terres-

trial laser scanner Riegl VZ-6000 on 23–25, 27, 30, and 31 August, and 1–3 September. On 24, 25, 27, 30, and 31 August, and 1 September, a series of frequently repeated (5–30 minutes interval) lidar surveys of the ice front, restricted to the southern half of the terminus, were made. Lidar Pulse Repetition Rate (PRR) was always set to 50 kHz and horizontal and vertical angular

5 resolution was typically set to $\sim 0.004°$. The lidar signal reflected from the northern part of the terminus was too weak to provide a reliable DSM due to large distance and, additionally, it was partially occluded from view by the protruding portion of the ice cliff near the centerline.

Resulting point clouds were preprocessed in Riegl RiSCAN-PRO software. Geocoding was made with a Multi Station Adjustment (MSA) plugin using ice-free areas of lidar scans of acquired from two auxiliary scan positions: one located near

10 KRBN array and second to the west of the main camp. Lidar positions were measured with static observations of differential GPS (Leica GS14) using NYA1 as a reference station. Subsequently, all the point clouds were aligned to a common reference frame using an iterative closest point (ICP) algorithm. Multiple cloud alignment yielded mean global positioning error of 8 cm. Each resulting point cloud was cropped to the ice cliff face by manual removal of the points related to the floating icebergs and boats. Point clouds were processed with Cloud Compare software in which horizontal mismatches between sequential point

15 clouds was removed using the M3C2 plugin (Lague et al., 2013). Results were projected to a new gridded point cloud with a fixed spatial resolution of 10 cm. Then, it was separated into two classes based on the sign of the distance change between sequential point clouds: ice terminus was classified as affected by calving when the change was positive, i.e. the distance from lidar scanner to the ice front increased due to calving; where the sign was negative, ice front advanced. Sub-clouds classified as affected by calving were segmented to particular calving events with the method of Awrangjeb (2016) that employs maximum

20 point-to-point distance in the input data to classify boundary edges. Calving event scars have low reflectance in near infrared part of spectrum used by lidar and this causes a decrease in point cloud density. Therefore, total volume of a calving event was calculated as a product of calving scar area and average calving event depth. Owing to short time between subsequent lidar acquisitions (<1 hour), ice advection was neglected as front advance during such time difference is much lower (1–6 cm) than calving event depth (meters). For inter-daily point cloud differencing, front advance related to ice advection that takes place

25 between measurements cannot be neglected. Hence, in such case the approach of Pętlicki and Kinnard (2016) was used, where point cloud differences in adjacent areas not affected by calving (ice advection) is added to the displacement caused by calving.

3 Detection, location, and validation of calving signals

Seismic arrays allow detecting weak seismic signals and suppressing uncorrelated noise by beamforming (Schweitzer et al., 2012). Frequency-Wavenumber (FK) analysis for example allows measuring the direction towards the signal source (back-

30 azimuth) through maximizing the stacked, travel-time corrected spectral amplitudes, the so called absolute beampower. Array analysis is in particular useful for calving events at Kronebreen, since these signals do not exhibit clear P and S wave onsets required for travel-time-based epicenter inversion (Köhler et al., 2015).

We compute a time series of absolute FK beampowers in 1 s long time windows with 50% overlap for each array between 1 and 3 Hz, the predominant frequency band of seismic calving signals at Kronebreen (Köhler et al., 2015). Subsequently,
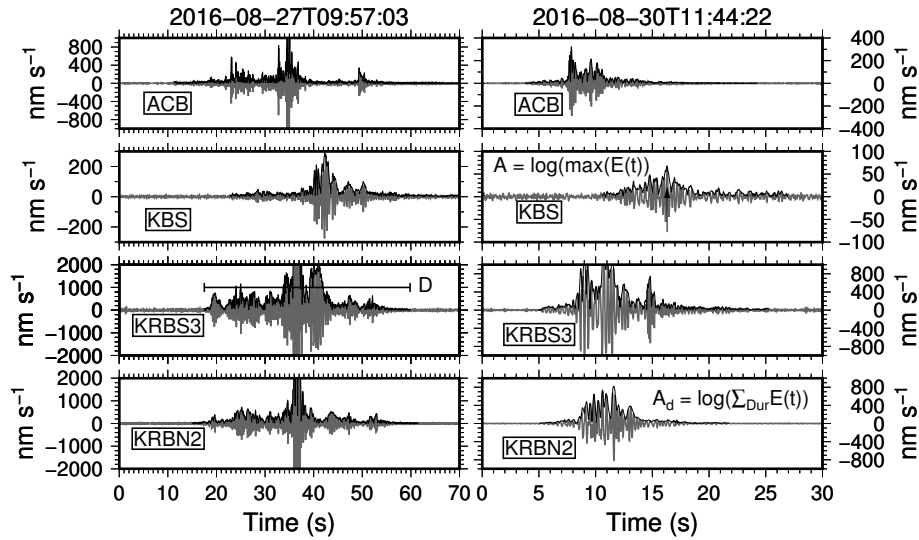
Figure 2. Examples of hydroacoustic (ACB) and seismic (KBS, KRBN2, KRBS3) signals of two calving events. Waveforms are bandpass-filtered between 2 and 12 Hz are shown in grey. Black curves are signal envelopes ($E(t)$) used to compute the event features: signal duration (D), logarithm of envelope amplitude integrated over event duration (A_d), and logarithm of maximum envelope amplitude (A).

a short-term over long-term average (STA/LTA) trigger (Withers et al., 1998) is applied independently to both beampower time series (STA=2 s, LTA=20 s, threshold=6). An event is declared if the STA/LTA threshold is exceeded on both arrays. The STA/LTA parameters are found through visual evaluation of selected seismogram time windows. The detections are then

5 located using the spatial mapping by multi-array beamforming method (SMAB, in supplementary information in Köhler et al., 2016). The SMAB method assumes a straight ray path from the source to each array stations, a condition we find not to be sufficiently fulfilled, most likely due to 2D propagation effects along the ice–ocean–land interfaces. We therefore empirically correct for the azimuthal bias observed at each array during SMAB processing (see Appendix and Fig. B1 for details).

A relatively large location uncertainty is expected given the long wavelength of seismic calving signals (λ = 400–1000 m),

10 limiting the spatial resolution of array beamforming to not less than 100–250 m ($\lambda/4$ criterion). Furthermore, seismic propagation effects not explained by the azimuthal correction can contribute to the overall location uncertainty. A conservative estimate of the average uncertainty is 320 m (longitude) and 260 m (latitude) (Fig. 1c) which are the medians of the difference between individual SMAB locations (longitude / latitude coordinates) and directly observed calving location from the time-lapse imagery (see scatter plot Fig. B1c). For further processing, we select all events with normalized SMAB beampower $>$0.5 and

15 with source locations inside a box around the terminus of Kronebreen (box dimension: $12.54\,°E <$ lon $< 12.68\,°E$, $78.848\,°N <$ lat $< 78.8926\,°N$, see Fig. 1c). Comparison with time-lapse images shows that a few calving events are detected as two or more separated seismic signals. Therefore, consecutive signals in our catalog are merged in a post-processing step if seismic locations are less than 400 m away from each other along the calving front and the detection time difference is less than 10 s.

The seismic record of the permanent station KBS has been previously used to generate a catalog of calving events between 2001 and 2015 (Köhler et al., 2016). For this study, we updated this catalog by processing data of recent years (2016–2017) using the same detection method. The calving event classifier for KBS was retrained using seismic signals from 2016 confirmed to originate at Kronebreen using our temporary seismic deployment and the time-lapse images. KBS detections during the field

5 experiment are shown in Fig. 1b (gray histogram).

In total 1,460 seismic calving event signals are simultaneously detected on array KRBN and KRBS within the measurement period. As expected, the detection rate is affected by the seismic background noise level, i.e., less events are being detected during windy time periods when for example ocean waves generate more ambient vibrations (Fig. 1b). The majority of seismic detections are visually confirmed on time-lapse camera images. Visual inspection of time-lapse images for all events on 30

10 August reveals that only 4% of all seismic detections located within the camera-covered range of the terminus cannot be visually confirmed (false positives). Most non-confirmed signals (16% of the total number of detections) originate from outside the camera range at the southern end of the terminus, or are concealed from the observer as a result of the front geometry. We also assess the possibility of missed calving events (false negatives) using the catalog of events independently obtained from time-lapse camera images (see Appendix and Fig. 1a). Only 7% of all events caught on camera cannot be matched with a

15 simultaneous seismic detection on both arrays. However, weak seismic signals can be identified on one of both arrays for many of those events. Since we require detection on both arrays for a more accurate location, we do not include these events in further processing. Days of high seismic noise level (25 and 28 August) account for more than 50% of these false negatives. Depending on the noise level, between 10 and 45% of all calving signals observed on the arrays at Kronebreen are detected at the permanent station KBS, consistent with an earlier experiment conducted in 2013 (Köhler et al., 2016).

4 Model development, calibration, and results

To find a relation between seismic calving signals and measured ice volumes, we compute the following features for each detection after bandpass-filtering between 1.5 and 5 Hz (Bartholomaus et al., 2015; Köhler et al., 2016): signal duration (D), logarithm of envelope amplitude integrated over event duration (A_d), and logarithm of maximum envelope amplitude (A). After testing all sensor records, we decided to use a single station of each array exhibiting the best signal-to-noise ratio (KRBN2,

25 KRBS3). Furthermore, we use the seismic detection times to extract the corresponding calving signals from the record of the hydrophone located closest to the calving front (ACB, Fig. 1c) and compute the same features as for the seismic signals. Although hydroacoustic data provide a much broader frequency range, we find the computation of features below 15 Hz to be most robust for calibration to ice volumes. The reasons are underwater noise level being in general higher and calving-related signals tending to be less well-defined and localized in time at higher frequencies. We find that hydroacoustic calving signals

30 often consist of multiple arrivals and weak signals emitted in the aftermath of the ice–water impact, possible caused by ice avalanches at the terminus, ice breakup at the calved ice block, and air bubble noise from melting freshly calved ice (Urick, 1971; Tegowski et al., 2014; Pettit et al., 2015). Figure 2 presents signals of two typical calving events on KRBN2, KRBS3, ACB, and KBS with signal envelopes shown as black curves.
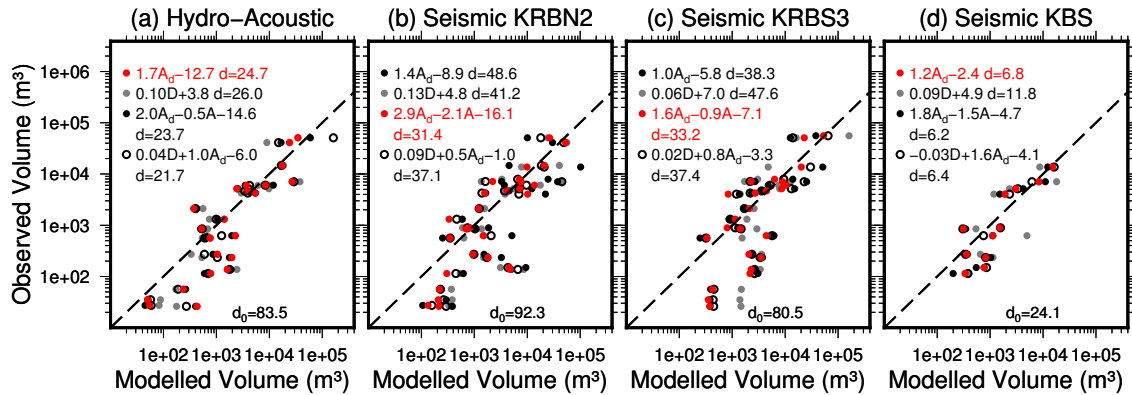
Figure 3. GLMs relating waveform properties to calving volume (lidar scanning) of individual events. Models are calibrated for different stations and combination of calving signal features (D: signal duration, A_d: amplitude integrated over event duration, A: maximum amplitude). Model coefficients, deviance (d), and Null deviance (d_0) of each model are stated. Red symbols show selected models.

From repeated lidar scans with 30 minute intervals at daytime on 24, 25, 27, 30, and 31 August, and 1 September, we obtain 100 individual calving volumes. Three sources of uncertainty exist when matching these volumes with the corresponding seismic and hydroacoustic calving signals: (1) The lack of exact timing in the lidar catalog, i.e., we only know that the event occurred within the scanning interval, (2) the assumption that a volume measured at a particular location corresponded to a single event, not to multiple events spread out within the scanning interval, and (3) the seismic location uncertainty. In other words, we have accurate timing but uncertain locations in case of seismic observations, and uncertain timing but precise locations for events in the lidar catalog. The time-lapse camera images are thus used to manually identify as many high-confidence matches between the seismic and the lidar catalog as possible. For each seismic calving event, the corresponding camera image series are inspected, and the location of the calving event at the terminus is visually identified. We then select all events from the lidar catalog during the scanning interval including the seismic signal at this location. Doing so, we take into account the location of the laser scan focus at the seismic detection time. Lack of continuous images due to camera failure on 27 and 31 August, and 1 September reduces the number of usable lidar volumes to 88, from which we are only able to unambiguously match 35 events. Unsuccessful matching is mostly due to events that occurred outside the camera range at the southernmost part of the terminus or due to the presence of too many candidates for matching. In a few cases, several isolated volumes with close proximity to each other correspond to a single calving event, i.e., to a single seismic signal. These volumes are merged accordingly. Furthermore, several calving events can occur at the same location during the scanning interval. In this case, we merge the corresponding seismic signals and treat them as a single event. This merging is done iteratively. We first calibrate signal properties to ice volumes excluding those signals and then re-calibrate our regression model using signal features merged according to the preliminary model (see below for more details). The final number of calving events available for calibration is 27 for the seismic and 22 for the hydroacoustic data. Since only the largest calving events are observed at 15 km distance, this number reduces to 12 events for the KBS record.

Following the approach of Bartholomaus et al. (2015), we use Generalized Linear Models (GLMs, McCullagh and Nelder, 1989) and test different combinations of features computed from the seismic or hydroacoustic calving signals to find an empirical relation to estimate the lidar calving volumes. The linear combination of predictor variables (seismic or hydroacoustic features) is related to the response variable (calving volume V) through a logarithmic link function. As in Bartholomaus et al. (2015) and Köhler et al. (2016) we employ the Gamma distribution to model the response variable. The GLMs have the form:

$$\log(V) = c_1 \cdot S_i + c_2 \cdot S_j + c_0, \tag{1}$$

where $c_{0,1,2}$ are the time-invariant model coefficients and S_i/S_j are chosen from the features D, A_d, and A computed from the hydroacoustic (ACB) and seismic calving signals (KRBN2, KRBS3, and KBS). Merging k multiple signal features for a single volume measurement as mentioned above is done by computing:

$$S_{merged} = (\log\Big(\sum_k \exp(c_1 \cdot S_k + c_0)\Big) - c_0)/c_1, \tag{2}$$

where c_0 and c_1 are obtained from a preliminary model trained using a single predictor variable (the feature to be merged) and without using the to-be-merged calving signals. Subsequently, the GLM is re-estimated including merged signals.

Figure 3 shows the results for 16 models using a single (c_2=0) or two predictor variables (see also Fig. C1). The GLM performance is evaluated using the deviance, the common quality-of-fit statistic for GLMs (McCullagh and Nelder, 1989). The Null deviance d_0 stated in Fig. 3 is the statistic for regression using a single model parameter c_0. In addition, the significance of model coefficients c_1 and c_2 to be non-zero is assessed using a T-test with 90% confidence. Finally, we perform a cross-validation test where we divide the data set randomly into 80% training and 20% validation data. This is repeated 500 times, and the mean of all RMS errors is computed.

Using deviance, cross-validation RMS errors, and T-test, we identify one or two best-performing models for each station (highlighted in red in Fig. 3). The results show that A_d alone or in combination with A tends to perform best for all stations. In case of the seismic data, combining A_d and A results in better models than using a single variable, with model coefficient c_2 for A always being negative. An intuitive explanation for this result is that A removes the effect of short-time amplitude spikes in the calving signal from the quantity A_d. These spikes might be caused by secondary processes during calving that are not directly related to the impact of the total ice volume into the water (e.g., ice projectiles, effects of the geometry of ice block, etc.).

Scatter between observed and predicted event volumes could be related to different factors affecting seismic and acoustics signals properties. i.e., source effects, such as the type of calving, shape of ice block, and/or manner of impact, as well as wave propagation effects depending on the travel path from different locations at the calving front to the receiver. We find that model performance does not improve significantly after including proxies for these effects. For example, multiplying A_d and A with the square root of the source distance to account for geometrical spreading (assuming surface waves), modeling the potential energy of the calved ice block instead of the ice volume to take into account fall height, or including the seismic/acoustic noise

level as an additional predictor variable since it can affect the measured length of a calving signal, does not improve the model fit.

5 Model validation with cumulative ice loss from lidar scans

Our results clearly show the existence of an empirical relation between calving signals properties and logarithm of ice volumes approximated by a linear trend. To validate our empirical models calibrated with individual, successfully matched calving events (i.e., a subset of all lidar ice volumes), we employ the cumulative subaerial ice loss measured from lidar scanning within
5 different time periods as a test data set. The sum of volumes over all scans during daytime on individual days as well as volumes obtained from the inter-daily scans are used.

First, we apply the best empirical models of each station obtained from the full calibration data (Fig. 3) to estimate the cumulative calving volume using all calving signals observed during the measurement period from 24 August until 2 September (white symbols in Fig. 4). In a second step, in order to estimate its uncertainty, we randomly select 80% of the calibration data
10 set to determine a new GLM M_{cv}. Then, the cumulative calving volume V_{cv} of all observed calving events is computed using M_{cv}. This is repeated 100 times. Figure 4 shows the resulting histograms plots for V_{cv} for all sensors. The distribution gives an impression about the uncertainty of the estimated total ice loss. Since the hydroacoustic recording period is shorter, we repeat this processing for the seismic data within the corresponding time period (gray histograms). Assuming a normal distribution for V_{cv}, the means and standard deviations are computed for each station to quantity the uncertainty of the total calving volume
15 estimate (Table 1).

Using all seismic calving observations at KRBN and KRBS during the field experiment, the total ice volume lays consistently for both models between $2 \cdot 10^6$ and $6 \cdot 10^6$ m^3 (Fig. 4, Table 1). Furthermore, V_{cv} values from the hydroacoustic data are in agreement with seismic data in the corresponding time period (Fig. 4). The volumes obtained from KBS lays between $0.5 \cdot 10^6$ and $1.5 \cdot 10^6$ m^3, suggesting that calving observed seismically at a distance of 15 km only accounts for about 25% of the ice loss
20 estimated close to the glacier. For comparison, the ice loss at Kronebreen measured with Lidar scanning between 24 August and 3 September is $2.7 \cdot 10^6$ m^3. Since parts of the calving front were not scanned, the actual volume is expected to be higher, which is consistent with the higher values obtained from our GLMs. Figure 5 shows a comparison between modeled and observed cumulative volumes for different lidar scanning intervals taking into account only seismic/hydroacoustic signals that occurred inside the actually scanned region (see also Table 1). There is a good correspondence with respect to the magnitude of obtained volumes. However, especially for inter-daily time intervals, our models tend to overestimate the ice loss, which reflects the general model uncertainty. As expected, ice volumes are underestimated at KBS since only a fraction of calving signals is observed at larger distance.
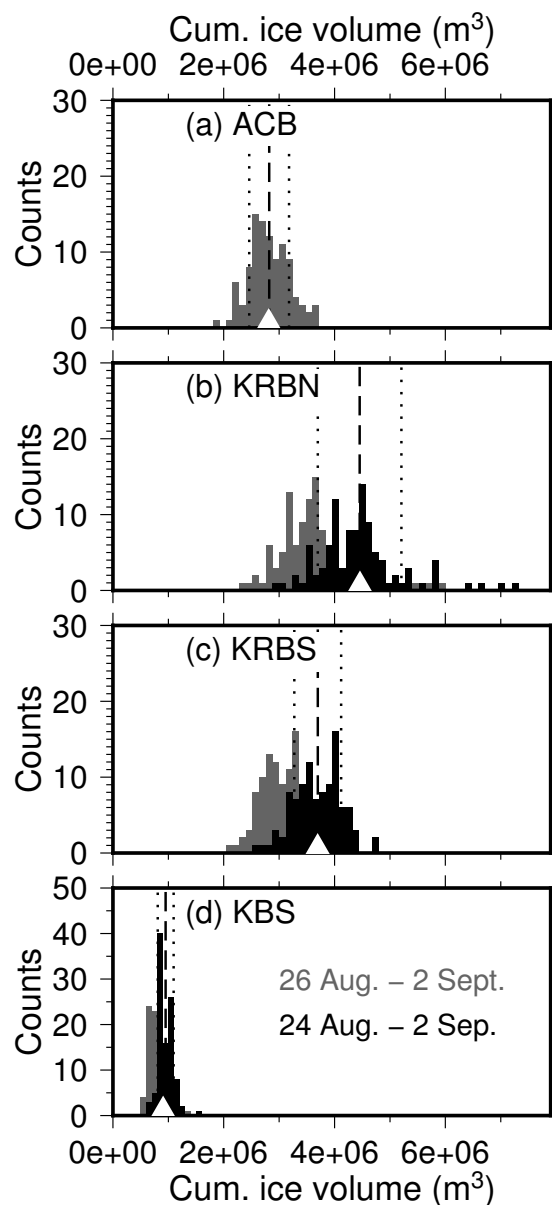
Figure 4. Modeled distribution of cumulative ice volumes between 24 August and 2 September using best GLMs in Figure 3 that are trained with 80% (randomly selected) of the calibration data in 100 runs (black histograms). White symbol is volume obtained with model calibrated with full data set. Grey histograms correspond to hydroacoustic recording period (from 26 August). Vertical lines indicate means (dashed) and standard deviation (dotted) obtained from the volume distribution.
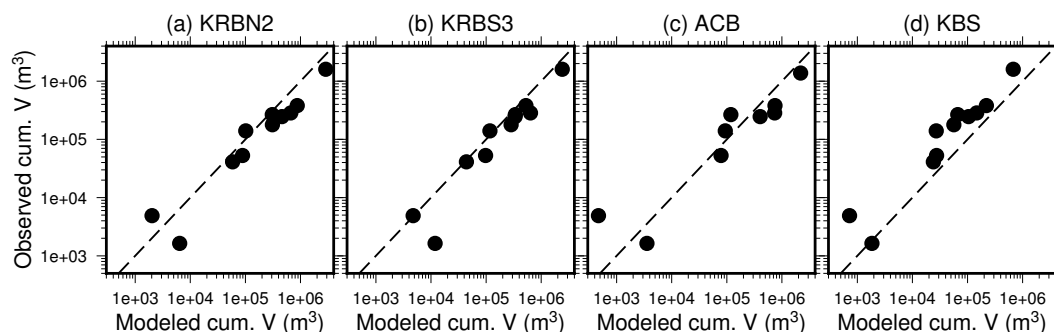
Figure 5. Modeled vs. observed cumulative volume for different lidar scanning intervals and stations in 2016 calibrating period.

Interval	Measurement	Obtained from seismic/hydroacoustic records with empirical models				
	Lidar	KRBN	KRBS	ACB	KBS	FA
25 Aug daytime	41.19	58.58	43.92	-	23.96	-
27 Aug daytime	52.78	88.66	97.72	78.72	27.50	-
30 Aug daytime	1.64	6.41	11.90	3.56	1.84	-
31 Aug daytime	4.89	2.03	4.74	0.47	0.72	-
1 Sep daytime	139.87	101.36	117.22	93.88	27.01	-
24-25 Aug	178.42	309.61	284.24	-	56.39	-
25-27 Aug	265.76	307.01	338.60	118.17 [1]	66.46	-
27-30 Aug	285.03	665.77	640.05	737.20	146.58	-
30-31 Aug	381.29	872.13	528.40	750.04	220.39	-
31 Aug - 1 Sep	245.75	460.57	336.69	402.75	104.41	-
24 Aug - 2 Sep [2]	2,737.12	4,500±800	3,700±400	2,800±400 [1]	950±140	18,000±2,000
2016	-	-	-	-	28,000±5,000	640,000±80,000

Table 1. Cumulative dynamic ice loss modeled and measured (Lidar) for different time intervals in units of 10^3 m^3. Only calving signals originated in the scanned range of terminus are used. FA: Frontal ablation (including submarine calving and melt) obtained from Köhler et al. (2016). [1] Acoustic data available from 26 Aug. [2] Lidar volume until 3 Sep and using all calving signals (entire front).

6 Comparing dynamic ice loss and total frontal ablation

In Fig. 6 we compare cumulative weekly dynamic ice loss obtained from our models with the total frontal ablation (which includes frontal melting) measured directly with satellite remote sensing data between 2007 and 2013 as well as modeled from the seismic KBS record between 2007 and 2017 (Köhler et al., 2016). A pronounced increase in modeled calving ice loss after 2013 is apparent, coinciding with the recent accelerated retreat of Kronebreen (Deschamps-Berger et al., 2019). Our results show an increase of dynamic ice loss rates, and also suggest longer calving seasons in recent years. The annual frontal ablation had values typically between 200 and 500·10^6 m^3 within the past 15 years (Köhler et al., 2016; Schellenberger et al., 2015).
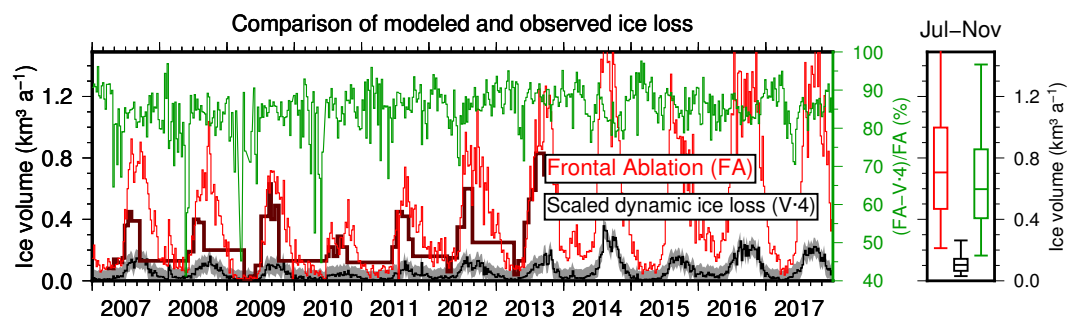
Figure 6. Comparison of frontal ablation rates at Kronebreen directly measured with satellite remote sensing between 2007 and 2013 (dark red) and modeled in Köhler et al. (2016) from seismic KBS data with weekly resolution (red). Scaled dynamic ice loss rates modeled in this study from KBS record and taking into account an average dynamic ice loss detection rate of 25% at KBS are shown in black with gray area indicating uncertainty (two times standard deviation estimated in 2016 calibration period, Table 1). Green curve is percentage of total frontal ablation not explained by modeled dynamic ice loss. Right panels shows box plot for calving season (2%, 25%, 98%, and 75% quantiles) using difference (FA-4·V) instead of percentage.

Dynamic ice loss modeled from KBS data in this study for the same time period shows as expected much lower rates (Fig. 6). As shown in the previous section, only a fraction of all subaerial calving events is observed at KBS due to significant seismic amplitude attenuation at 15 km distance. The percentage of detected events varies over time since noise level and possibly also the relative contribution of small vs. large calving events may change. Within our calibration period the variation

15 of completeness causes the modeled ice loss to vary between 15 and 58% of the measured values (see Table 1). Assuming an ice loss detection rate of 25%, comparison between ice loss modeled in this study and frontal ablation estimated in Köhler et al. (2016) suggests that between 70 and 95% of the frontal ablation does not occur through the physical process of iceberg calving (green curve in Fig. 6).

For the time period of our experiment between 24 August and 2 September, the approach of Köhler et al. (2016) yields

20 an ice loss of about $18 \cdot 10^6 \, \mathrm{m}^3$. Since about two-thirds of the grounded vertical terminus area of Kronebreen are submarine (Lindbäck et al., 2018) and assuming that submarine ice loss occurs mainly through melting as suggested by our visual calving observations at Kronebreen and How et al. (2019), the corresponding dynamic ice loss would be $6 \cdot 10^6 \, \mathrm{m}^3$ which is just slightly above the values estimated from the KRBN and KRBS records in this study, i.e., the contribution of calving to frontal ablation would be 18-30% (Table 1). For the entire year of 2016, the approach of Köhler et al. (2016) yields an ice loss of

25 about $640 \pm 80 \cdot 10^6 \, \mathrm{m}^3$. Taking again into account varying seismic catalog completeness at KBS resulting in underestimation of calving volumes (15 - 58% of true ice loss) and assuming that only subaerial ice loss contributes (about 33%), we would expect to obtained with our model for KBS between 5 and 20% of the actual frontal ablation, i.e., values within a range of 30 to $130 \cdot 10^6 \, \mathrm{m}^3$. In fact, we obtain $28 \pm 5 \cdot 10^6 \, \mathrm{m}^3$ in this study. Being located at the lower bound of the expected range is consistent with the contribution of dynamic ice loss to frontal ablation estimated above and might be related to a lower calving catalog

30 completeness during the fall, when calving usually continues with high activity, but frequent storms increase the amplitudes

of ambient seismic noise in the Kongsfjord area. Furthermore, the model of Köhler et al. (2016) was calibrated for the time period 2007–2013 which could result in a higher uncertainty or a bias in 2016.

7   Discussion

A major novelty of our approach, estimating iceberg volume directly from seismic or hydroacoustic calving signals, is that a source of uncertainty in the empirical model is removed. Instead of qualitatively estimating the relation between visually perceived calving sizes in the field and the actual volume as previous studies did, we use precise lidar scanning of the calving front for calibration. Our results clearly show that this approach works. The choice of the regression method (GLM) and calving signal features is similar and builds upon to the method presented by Bartholomaus et al. (2015). We confirm that the length of the signal represents the ice volume better than the maximum amplitude (Qamar, 1988; O'Neel et al., 2007b; Bartholomaus et al., 2015; Köhler et al., 2016). However, in contrast to previous studies, we find that empirical models using the integrated amplitude perform better than using the signal duration only. The difference of our approach compared to estimating frontal ablation from seismic calving records in Köhler et al. (2016) is a higher temporal resolution and the focus only on dynamic ice loss through modeling volumes of individual calving events. Therefore, our models do not use a time-normalized sum of seismic signal properties and the catalog incompleteness in specified time periods as predictor variables as done in Köhler et al. (2016).

7.1   Applicability and opportunities of seismic calving quantification

By calibrating a model for the permanent seismic station KBS in the vicinity of Kronebreen, our method allows a unique quantitative long-term monitoring of calving which is necessary to predict how glaciers will respond in a warming climate. Given that calibration experiments have been carried out, this approach can be applied to other similar situations worldwide where permanent seismic stations have been installed in the vicinity of a tidewater glacier. In our case, small and moderate-sized calving events are not detected and the long-time event catalog might be contaminated by calving signals from other glaciers in the region because KBS is located at 15 km distance and using a single station limits location accuracy. However, our results for the short-time record show that our calving quantification approach benefits from instruments deployed closer to the terminus and/or small-scale seismic arrays that allow better location and detection of weak calving signals.

Frontal ablation can be directly measured through satellite remote sensing or obtained from seismic records with empirical models and weekly resolution (Köhler et al., 2016). Combining these observations with dynamic ice loss estimates as presented in this study offers the potential to investigate the contribution of frontal melting to total frontal ablation. For example, we can compute an estimate for ice loss through melting from our modeled dynamic ice loss and frontal ablation at Kronebreen by taking into account the (constant assumed) seismic catalog incompleteness at station KBS (Fig. 6). The magnitude and temporal variability of this non-dynamic ice loss, however, is affected not only by variation of frontal melt, but also by changing catalog completeness, i.e., more weak signals remain undetected if background noise increases, which in theory can also include changing contribution of undetected submarine calving. Hence, variations in the computed contribution of the frontal melting

proxy have to be interpreted with caution. Using the method to asses to calving catalog incompleteness at KBS suggested by Köhler et al. (2016) would in theory allow distinguishing between variations in calving and variations in noise. This would be a major step forward in better understanding processes at ice–ocean interfaces. Deploying instrument arrays close to the glacier terminus, as done during our experiment in 2016, but for long-term monitoring makes seismic/hydroacoustic catalog completeness less an issue. Nevertheless, apart from limited capability to asses its temporal variability, we are able to give an estimate for the average contribution of dynamic ice loss to frontal ablation at Kronebreen of 5-30% (Fig. 6, right panel). This implies and confirms recent studies that water temperature is the main driver of frontal ablation through underwater melting and thermal undercutting which in consequence controls subaerial calving (Bartholomaus et al., 2013; Luckman et al., 2015; Vallot et al., 2018; How et al., 2019). Using the cross-sectional submarine area (2.3 and 2.9 km^2 in 2009 and 2014, respectively), our residual frontal melting component of Kronebreen would imply a retreat rate of 150–350 m a^{-1} due to these processes alone. This is reasonable given the front position behavior and horizontal velocity measured over the past decade (Schellenberger et al., 2015; Luckman et al., 2015).

We calibrate our models with subaerial calving events. It is well-known that also submarine calving generates underwater acoustic and weak seismic signals. Glowacki et al. (2015) showed that hydroacoustic calving signals at Hansbreen, southern Svalbard, allow distinguishing submarine and subaerial calving events based on spectral characteristics. However, at Kronebreen we found it difficult to distinguish the seismic calving signals from subaerial and submarine calving. Seismic signals from submarine events are in general weaker, but are often indistinguishable from weak subaerial calving events or occur simultaneously with those. Hence, calving at the submarine part of the terminus is partially included in our modeled ice volumes, but could be underestimated if we assume the corresponding low-amplitude signals to be subaerial. This is similar to the effect of increasing seismic background noise level which results in an apparent shorter duration of the calving signal. However, we observe only a few percent of all calving events to be submarine in the time-lapse images, and therefore have good evidence that our ice loss estimates are not significantly affected. This is supported by recent observations made by How et al. (2019) at Tunabreen, a tidewater glacier in central Svalbard, where 97% of all calving events occurred subaerially, even though 60–70% of the terminus is below sea level, similar to Kronebreen.

7.2 Potential model extensions

Being limited by a low number of calibration data, seismic and lidar records acquired over a longer time period will offer the potential to further improve our empirical models by reducing prediction uncertainty. Since we encountered challenges related to matching lidar volumes and calving signals when calving within the scanning interval occurs frequently, we will scan multiple smaller areas in future field experiments to unambiguously relate more calving events and their signals. This was already tested during the last days of our experiment using a single scanner and a repetition rate up to 5 min. However, the measurement period was not long enough to capture a sufficiently high number of calving events. Another possible solution is to derive ice volume from a multiview structure-from-motion photogrammetry with a multiple time-lapse camera array (Mallalieu et al., 2017). This method allows for higher temporal resolution and is much more economic than lidar scanning, however, it requires a favorable geometry setup that is hard to meet for tidewater glaciers. Another approach which we tested

and which provides more calibration data is to measure calving areas from time-lapse images extracted at the seismic detection times and then scale to volumes using an empirical relation between camera-measured areas and lidar volumes. However, similar to the method using visually quantified calving volumes, two empirical models have to be combined which results in a larger prediction uncertainty.

Our calving volume estimates of individual events include uncertainty since the calibration data set is limited and not all parameters affecting the calving signals can be modeled yet in the regression. The interaction between ice and water during calving is complex, and it is therefore not surprising that signal features have limited predictor ability for the volume. Ultimately, physical models such as proposed by Bartholomaus et al. (2012) or numerical modeling of the ice–water impact would be required to better understand seismic/hydroacoustic signal generation. Furthermore, our empirical models are valid for a particular calving style mainly observed in Svalbard, Alaska, and South America where most seismic calving signals are generated by the impact of the iceberg in the fjord (Bartholomaus et al., 2012). In contrast, the glacier mass loss through calving in Greenland and Antarctica is dominated by the breakup of large tabular icebergs representing a different type of seismic source mechanism (Murray et al., 2015). Determination of calving sizes from those seismic calving signals (glacier earthquakes) may therefore require a different or more generalized approach.

Our models are calibrated for a particular glacier, terminus environment, and seismic/hydroacoustic sensor setup. Hence, application to seismic data acquired at a different glacier requires carrying out a new calibration experiment. A potential solution to make empirical models adaptable for different glaciers is to introduce site-specific predictor variables such as source distance, noise level, calving front geometry, water depth, and other seismic wave propagation properties (site and path effects). This approach requires a larger number of calibration data points to prevent overfitting in the regression as well as field campaigns at several glaciers carried out over longer recording periods than 1–2 weeks at each individual site.

8 Conclusions

Measuring glacier mass loss through calving continuously and with high temporal resolution is challenging. Seismic and hydroacoustic data recorded at the front of marine-terminating glaciers allow detection of calving signals with second-precision, but require calibration to actual ice volumes. We successfully developed empirical models relating calving signals to volumes at Kronebreen, a fast-flowing tidewater glacier in Northwest Svalbard, based on calving volumes from 10 days of repeat lidar scanning in August and September 2016. In addition to seismic data recorded at three different locations including a permanent station with a more than two decades-long record, we used for the first time a hydroacoustic record. For all records, the amplitude integrated over the calving signals in combination with the maximum amplitude allowed us to model the volumes of individual calving events. While seismic arrays are needed for calving event detection and location, underwater acoustic signals measured on a single sensor showed similar quality and predictor capability for ice volumes as their seismic counterparts and could therefore be used as an complementary record to asses model uncertainty. Reducing seismic calving model uncertainty will benefit from extended calibration data sets at multiple glaciers with shorter lidar scanning intervals and longer recording periods, which better take into account event- and site-dependent variables, and allow improving the matching process between

lidar and seismic calving observations. Application of our model showed that the cumulative ice loss estimated from seismic

30 and hydroacoustic data is consistent with measured ice loss in different lidar scanning intervals as well as with frontal ablation rates measured with satellite remote sensing.

Our method offers a promising approach to not only continuously measure calving ice loss with high temporal resolution, but also to indirectly measure frontal glacier melting by evaluating the contribution of dynamic ice loss to the frontal ablation. For the permanent station KBS we model between 15 and 60% of the dynamic ice loss observed close to the calving front since only a fraction of all calving event are detected at 15 km distance depending on seismic noise level. Taking this catalog

5   incompleteness into account allows for long-term monitoring of calving ice loss at Kronebreen. Comparison with total frontal ablation showed that dynamic ice loss contributed with 5-30% between 2007 and 2017. This implies a large component of frontal ablation is melting at the calving face, which we can estimate for Kronebreen in the same period to be roughly 150–350 m a^{-1}. Future work should consider analysis of higher temporal resolution variability of these estimates which will further unravel the controls on frontal ablation and will be beneficial for realistically modeling ice loss at marine terminating glaciers

10 in relation to both atmospheric and oceanic forcings.

Data availability. Data of station KBS are freely available through IRIS (Albuquerque Seismological Laboratory (ASL)/USGS, 1988). The seismic record of the temporary network stations will become freely accessible through the Geophysical Instrument Pool Potsdam (GIPP) after 1 October 2020 (Köhler et al., 2019).

Appendix A: Time-lapse camera image processing

15 The time-lapse images are first gathered per hour and corrected for lens distortion. The correction is based on the barrel method that follows the equation $R = r\left(a \cdot r^3 + b \cdot r^2 + c \cdot r + d\right)$ where R and r are the distances of the pixels from the centre of the original and corrected image, respectively (ImageMagick, Helmut Dersch). The parameters a, b, and c depend on the camera and lense type and are obtained from the opensource database Lensfun (Table A1). The parameter d is a scaling factor that is greater than 1 and compensates the cropping caused by the correction. The images are then rotated to have the

20 waterline horizontal, and applied a crop to only keep the front of the glacier. The parameters for the rotation and crop are manually identified and done every time the camera has moved significantly, usually after each maintenance. To compensate for rapid change in brightness due to environmental conditions or camera settings, we compute a histogram equalisation for each colour channel separately. This method linearises the cumulative distribution function of the pixel bins and enhance the contrast of the image. This luminosity correction performs better than stretching pixel values to their maximum range (e.g.

5 normalisation). The RGB image is then converted into a grayscale image Y based on a standard Luma compression so that $Y = 0.298839 \cdot R + 0.586811 \cdot G + 0.114350 \cdot B$. The constants are chosen to enhance spatial sensitivity of human vision. Other conversions may be used to enhance colours (i.e. blues), but were not tested here.

The calving detector is developed based on visual characteristics of calving. As the ice breaks off and hit the water, it causes a rapid jet of water and a long-term change in albedo and roughness of the glacier front. The detector aims to identify

5 these temporal variations in pixel brightness that occurs along the glacier and above the waterline. The method consists of stacking over time a line of pixel above the front waterline, computing the second derivative in time, apply a low-pass filter and detect events using a threshold value (Fig. A1). The time and location of each calving is retrieved and manually verified using reprocessed gifs of the calving front at these defined time and coordinates.
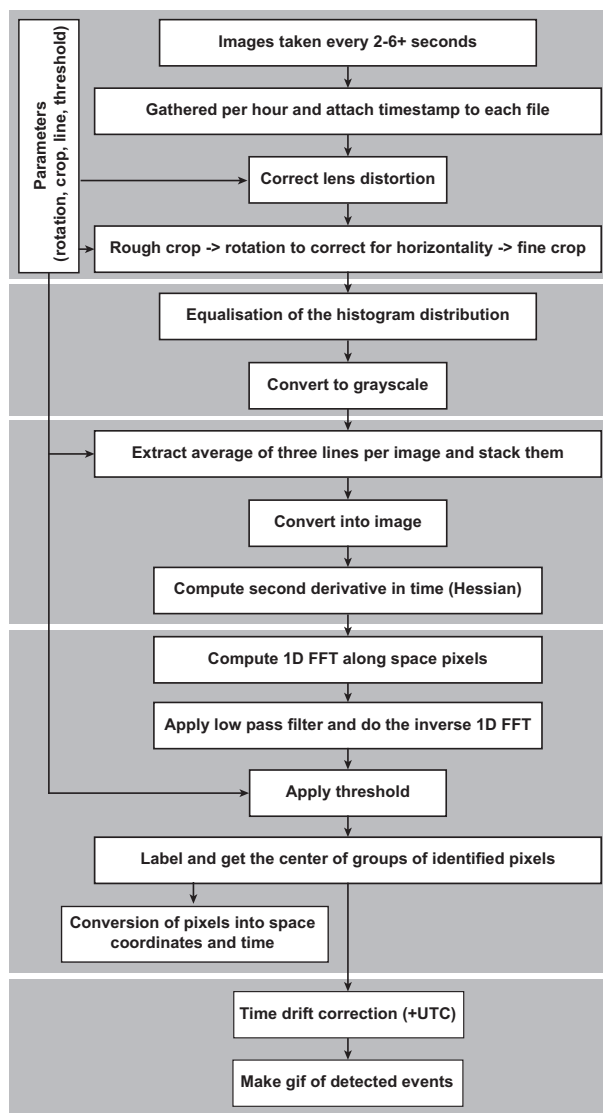
Figure A1. Workflow for detecting calving events in the time-lapse image data.

Table A1. Camera details and lense distortion parameters

Camera		Canon EOS	Canon EOS
Model		REBEL T3	1200D
Sensor	mm	22.2 x 14.7	22.3 x 14.9
Image size	px	4272 x 2848	5184 x 3456
Pixel	Mpx	12.2	18.1
JPG size	MB	2.5	6
Lense		Canon EF-S 18-55mm f/3.5-5.6 IS II	Canon EF-S 18-55mm f/3.5-5.6 III
Focal length		18	18
	a	0.02504	0.00029
Distortion	b	-0.06883	-0.00065
parameters	c	0.01502	-0.04054
	d	1.15	1.15
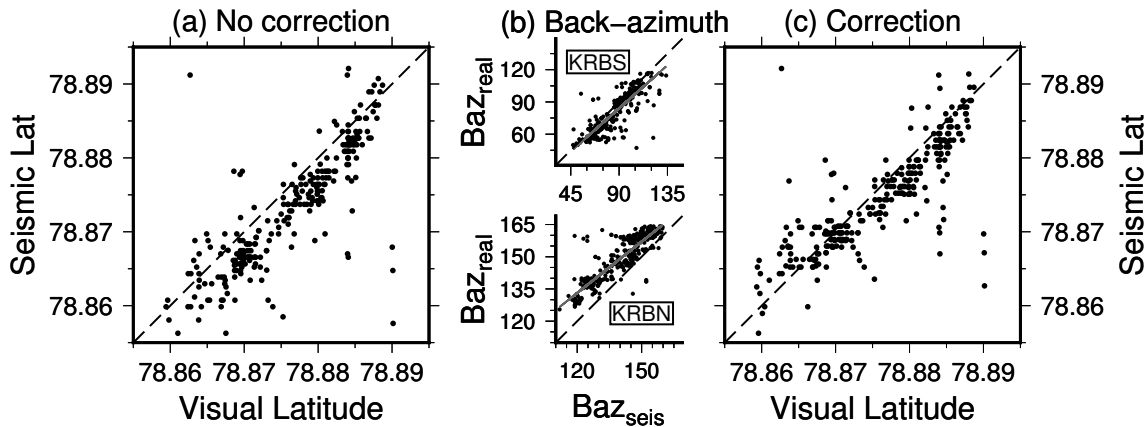
Figure B1. Latitude of calving events located from seismic signals vs. latitude of visually observed on time-lapse camera images. (a) No correction. (b) Back-azimuth of calving signals observed on both seismic arrays vs. visually observed. Grey line is results of a linear regression. (c) Same as in (a) but applying an empirical correction based on the regression in (b) correcting for observed back-azimuth bias.

Appendix B: Seismic back-azimuth correction

10 For seismic signals originating at Kronebreen a discrepancy is observed between back-azimuths measured with FK analysis (Baz_{seis}) and real back-azimuths Baz_{real} of calving events visually observed on the time-lapse camera images (Fig. B1b). For correction, a linear dependency of the form $Baz_{real} = a \cdot Baz_{seis} + b$ is assumed. The coefficients a and b are obtained by linear regression using all seismic calving signals confirmed on time-lapse camera images.
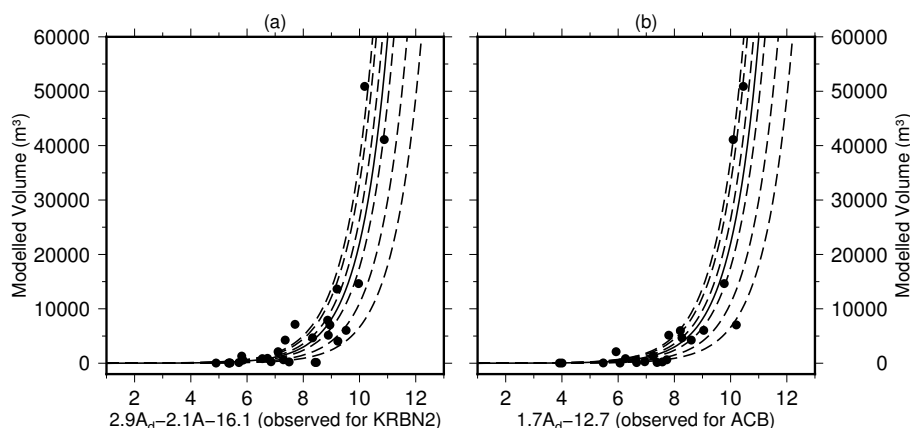
Figure C1. Best performing GLMs for KRBN2 and ACB. Symbols show calibration data. Solid line is fitted model. Dashed line show deviations of $\pm 20\%$, 50% and 70% for a given volume.

Appendix C: Model calibration

Fig. C1 shows a different visualization of two calibrated models shown in Fig. 3.

Author contributions. AK and CN initiated the study. AK processed and analyzed the seismic data, built and tested the models, and prepared

5   the manuscript. MP acquired and processed lidar data. PML acquired and processed time-lapse camera images. GB acquired and processed hydroacoustic data. CN was PI of the CalvingSEIS project and planned and organized logistics for the field experiment. CW was responsible for seismic field instrumentation and assisted in the field experiment. All authors contributed to manuscript writing and editing.

Competing interests. The authors declare that they have no conflict of interest.

Acknowledgements. This study was carried out in the framework of the CalvingSEIS research project funded by the Research Council of

10   Norway (244196/E10). Seismic instrumentation for temporary arrays was provided by the Geophysical Instrument Pool of GFZ Potsdam, Germany. We use obspy (Beyreuther et al., 2010) for seismic data analysis and statsmodel (Seabold and Perktold, 2010) for GLMs. Figures are produced using GMT (Wessel and Smith, 1998). MP acknowledges the support of the Centro de Estudios Científicos (CECs) funded by the Centers of Excellence Base Financing Program of the CONICYT-Chile.

References

15 Albuquerque Seismological Laboratory (ASL)/USGS: Global Seismograph Network (GSN - IRIS/USGS), https://doi.org/10.7914/sn/iu, 1988.

Amundson, J. M., Truffer, M., Lüthi, M. P., Fahnestock, M., West, M., and Motyka, R. J.: Glacier, fjord, and seismic response to recent large calving events, Jakobshavn Isbræ, Greenland, Geophysical Research Letters, 35, https://doi.org/10.1029/2008GL035281, http://dx.doi.org/10.1029/2008GL035281, L22501, 2008.

20 Aster, R. and Winberry, J.: Glacial seismology, Reports on Progress in Physics, 80, 39pp, https://doi.org/10.1088/1361-6633/aa8473, 2017.

Awrangjeb, M.: Using point cloud data to identify, trace, and regularize the outlines of buildings, International Journal of Remote Sensing, 37, 551–579, https://doi.org/10.1080/01431161.2015.1131868, 2016.

Bartholomaus, T., Larsen, C., O'Neel, S., and West, M.: Calving seismicity from iceberg–sea surface interactions, Journal of Geophysical Research, 117, https://doi.org/10.1029/2012JF002513, F04029, 2012.

25 Bartholomaus, T. C., Larsen, C. F., and O'Neel, S.: Does calving matter? Evidence for significant submarine melt, Earth and Planetary Science Letters, 380, 21–30, https://doi.org/10.1016/j.epsl.2013.08.014, 2013.

Bartholomaus, T. C., Larsen, C. F., West, M. E., O'Neel, S., Pettit, E. C., and Truffer, M.: Tidal and seasonal variations in calving flux observed with passive seismology, Journal of Geophysical Research: Earth Surface, 120, 2318–2337, https://doi.org/10.1002/2015JF003641, 2015.

Beyreuther, M., Barsch, R., Krischer, L., Megies, T., Behr, Y., and Wassermann, J.: ObsPy: A Python toolbox for seismology, Seismological
30   Research Letters, 81, 530–533, https://doi.org/10.1785/gssrl.81.3.530, 2010.

Chapuis, A., Rolstad, C., and Norland, R.: Interpretation of amplitude data from a ground-based radar in combination with terrestrial photogrammetry and visual observations for calving monitoring of Kronebreen, Svalbard, Annals of Glaciology, 51, 34–40, https://doi.org/10.3189/172756410791392781, 2010.

Deschamps-Berger, C., Nuth, C., Van Pelt, W., Berthier, E., Kohler, J., and Altena, B.: Closing the mass budget of a tidewater glacier: the
35   example of Kronebreen, Svalbard, Journal of Glaciology, pp. 1–13, https://doi.org/10.1017/jog.2018.98, 2019.

Ekström, G., Nettles, M., and Abers, G. A.: Glacial earthquakes, Science, 302, 622–624, https://doi.org/10.1126/science.1088057, 2003.

Gardner, A. S., Moholdt, G., Cogley, J. G., Wouters, B., Arendt, A. A., Wahr, J., Berthier, E., Hock, R., Pfeffer, W. T., Kaser, G., Ligtenberg, S. R. M., Bolch, T., Sharp, M. J., Hagen, J. O., van den Broeke, M. R., and Paul, F.: A reconciled estimate of glacier contributions to sea level rise: 2003 to 2009, Science, 340, 852–857, https://doi.org/10.1126/science.1234532, 2013.

Glowacki, O., Deane, G., Moskalik, M., Blondel, P., Tegowski, J., and Blaszczyk, M.: Underwater acoustic signatures of glacier calving, Geophysical Research Letters, 42, 804–812, https://doi.org/10.1002/2014GL062859, http://dx.doi.org/10.1002/2014GL062859, 2015.

5   How, P., Schild, K. M., Benn, D. I., Noormets, R., Kirchner, N., Luckman, A., Vallot, D., Hulton, N. R., and Borstad, C.: Calving controlled by melt-under-cutting: detailed calving styles revealed through time-lapse observations, Annals of Glaciology, pp. 1–12, https://doi.org/doi:10.1017/aog.2018.28, 2019.

Huss, M. and Hock, R.: A new model for global glacier change and sea-level rise, Frontiers in Earth Science, 3, https://doi.org/10.3389/feart.2015.00054, 2015.

10 Köhler, A., Nuth, C., Schweitzer, J., Weidle, C., and Gibbons, S. J.: Regional passive seismic monitoring reveals dynamic glacier activity on Spitsbergen, Svalbard, Polar Research, 34, 26 178, https://doi.org/10.3402/polar.v34.26178, 2015.

Köhler, A., Nuth, C., Kohler, J., Berthier, E., Weidle, C., and Schweitzer, J.: A 15 year record of frontal glacier ablation rates estimated from seismic data, Geophysical Research Letters, 43, 12 155–12 164, https://doi.org/10.1002/2016GL070589, 2016.

Köhler, A., Weidle, C., and Nuth, C.: Glacier dynamic ice loss quantified through seismic eyes (CALVINGSEIS) – Dataset, GFZ Data
Services, https://doi.org/10.5880/GIPP.201604.1, 2019.

Lague, D., Brodu, N., and Leroux, J.: Accurate 3D comparison of complex topography with terrestrial laser scanner: Application to the Ran-
gitikei canyon (NZ), ISPRS Journal of Photogrammetry and Remote Rensing, 82, 10–26, https://doi.org/10.1016/j.isprsjprs.2013.04.009,
2013.

Lindbäck, K., Kohler, J., Pettersson, R., Nuth, C., Langley, K., Messerli, A., Vallot, D., Matsuoka, K., and Brandt, O.: Subglacial
topography, ice thickness, and bathymetry of Kongsfjorden, northwestern Svalbard, Earth System Science Data, 10, 1769–1781,
https://doi.org/10.5194/essd-10-1769-2018, 2018.

Luckman, A., Benn, D. I., Cottier, F., Bevan, S., Nilsen, F., and Inall, M.: Calving rates at tidewater glaciers vary strongly with ocean
temperature, Nature communications, 6, https://doi.org/10.1038/ncomms9566, 2015.

Mallalieu, J., Carrivick, J. L., Quincey, D. J., Smith, M. W., and James, W. H.: An integrated Structure-from-Motion and time-lapse technique
for quantifying ice-margin dynamics, Journal of Glaciology, 63, 937–949, https://doi.org/10.1017/jog.2017.48, 2017.

McCullagh, P. and Nelder, J. A.: Generalized linear models, vol. 37, CRC press, 1989.

Murray, T., Selmes, N., James, T. D., Edwards, S., Martin, I., O'Farrell, T., Aspey, R., Rutt, I., Nettles, M., and Baugé, T.: Dynamics of
glacier calving at the ungrounded margin of Helheim Glacier, southeast Greenland, Journal of Geophysical Research: Earth Surface, 120,
964–982, https://doi.org/10.1002/2015JF003531, 2015.

Nuth, C., Schuler, T. V., Kohler, J., Altena, B., and Hagen, J. O.: Estimating the long-term calving flux of Kronebreen, Svalbard, from geodetic
elevation changes and mass-balance modelling, Journal of Glaciology, 58, 119–133, https://doi.org/10.3189/2012JoG11J036, 2012.

O'Neel, S., Echelmeyer, K. A., and Motyka, R. J.: Short-term variations in calving of a tidewater glacier: LeConte Glacier, Alaska, U.S.A.,
Journal of Glaciology, 49, 587–598, https://doi.org/10.3189/172756503781830430, 2003.

O'Neel, S., Marshall, H. P., McNamara, D. E., and Pfeffer, W. T.: Seismic detection and analysis of icequakes at Columbia Glacier, Alaska,
Journal of Geophysical Research, 112, https://doi.org/10.1029/2006JF000595, F03S23, 2007b.

O'Neel, S., Larsen, C., Rupert, N., and Hansen, R.: Iceberg calving as a primary source of regional-scale glacier-generated seismicity in the
St. Elias Mountains, Journal of Geophysical Research, 115, https://doi.org/10.1029/2009JF001598, f04034, 2010.

Pettit, E. C., Lee, K. M., Brann, J. P., Nystuen, J. A., Wilson, P. S., and O'Neel, S.: Unusually loud ambient noise in tidewater glacier fjords:
A signal of ice melt, Geophysical Research Letters, 42, 2309–2316, https://doi.org/10.1002/2014GL062950, 2015.

Pętlicki, M. and Kinnard, C.: Calving of Fuerza Aérea Glacier (Greenwich Island, Antarctica) observed with terrestrial laser scanning and
continuous video monitoring, Journal of Glaciology, 62, 835–846, https://doi.org/10.1017/jog.2016.72, 2016.

Podolskiy, E. A. and Walter, F.: Cryoseismology, Reviews of geophysics, 54, 708–758, https://doi.org/10.1002/2016RG000526, 2016.

Qamar, A.: Calving icebergs: A source of low-frequency seismic signals from Columbia Glacier, Alaska, Journal of Geophysical Research,
93, 6615–6623, https://doi.org/10.1029/JB093iB06p06615, 1988.

Schellenberger, T., Dunse, T., Kääb, A., Kohler, J., and Reijmer, C.: Surface speed and frontal ablation of Kronebreen and Kongsbreen, NW
Svalbard, from SAR offset tracking, The Cryosphere, 9, 2339–2355, https://doi.org/10.5194/tc-9-2339-2015, 2015.

Schweitzer, J., Fyen, J., Mykkeltveit, S., Gibbons, S., Pirli, M., Kühn, D., and Kværna, T.: Seismic Arrays, in: Bor-
mann, P. (ed.), New Manual of Seismological Observatory Practice (NMSOP-2). 2nd (revised) edition, http://ebooks.gfz-
potsdam.de/pubman/item/escidoc:43213:7, pp. 1–80, Potsdam: Deutsches GeoForschungsZentrum GFZ, 2012.

Seabold, S. and Perktold, J.: Statsmodels: Econometric and statistical modeling with python, in: Proceedings of the 9th Python in Science
Conference, pp. 57–61, 2010.

Tegowski, J., Deane, G., Blondel, P., Glowacki, O., and Moskalik, M.: An acoustical study of gas bubbles escaping from melting growlers, in: Proceedings of the 2nd International Conference and Exhibition on Underwater Acoustics, pp. 137–142, 2014.

Torsvik, T., Albretsen, J., Sundfjord, A., Kohler, J., Sandvik, A. D., Skarðhamar, J., Lindbäck, K., and Everett, A.: Impact of tidewater glacier retreat on the fjord system: Modeling present and future circulation in Kongsfjorden, Svalbard, Estuarine, Coastal and Shelf Science, https://doi.org/10.1016/j.ecss.2019.02.005, 2019.

Urick, R.: The noise of melting icebergs, The Journal of the Acoustical Society of America, 50, 337–341, https://doi.org/10.1121/1.1912637, 1971.

Vallot, D., Åström, J., Zwinger, T., Pettersson, R., Everett, A., Benn, D. I., Luckman, A., van Pelt, W. J., Nick, F., and Kohler, J.: Effects of undercutting and sliding on calving: a global approach applied to Kronebreen, Svalbard, Cryosphere, 12, 609–625, https://doi.org/10.5194/tc-12-609-2018, 2018.

Vaughan, D., Comiso, J., Allison, I., Carrasco, J., Kaser, G., Kwok, R., Mote, P., Murray, T., Paul, F., Ren, J., Rignot, E., Solomina, O., Steffen, K., and Zhang, T.: Observations: Cryosphere, in: Climate Change 2013: The Physical Science Basis. Contribution of Working Group I to the Fifth Assessment Report of the Intergovernmental Panel on Climate Change. T. F. Stocker, D. Qin, G. K. Plattner et al., Cambridge University Press Cambridge, United Kingdom and New York, NY, USA, 2013.

Walter, F., Amundson, J. M., O'Neel, S., Truffer, M., Fahnestock, M., and Fricker, H. A.: Analysis of low-frequency seismic signals generated during a multiple-iceberg calving event at Jakobshavn Isbræ, Greenland, Journal of Geophysical Research, 117, https://doi.org/10.1029/2011JF002132, 2012.

Wessel, P. and Smith, W. H. F.: New, improved version of GMT released, Eos, Transactions, American Geophysical Union, 79, 579–579, https://doi.org/10.1029/98EO00426, 1998.

Withers, M., Aster, R., Young, C., Beiriger, J., Harris, M., Moore, S., and Trujillo, J.: A comparison of select trigger algorithms for automated global seismic phase and event detection, Bulletin of the Seismological Society of America, 88, 95–106, 1998.